Recent Progress of Microbubble Flow Simulation for Elucidating Drag Reduction Mechanism

Kazuyasu SUGIYAMA*, Takafumi KAWAMURA**, Shu TAKAGI*** and Yoichiro MATSUMOTO***

*Center for Smart Control of Turbulence, National Maritime Research Institute
6-38-1, Shinkawa, Mitaka-shi, Tokyo, 181-0004, JAPAN
**Department of Environmental and Ocean Engineering, The University of Tokyo
7-3-1 Hongo, Bunkyo-ku, Tokyo, 113-8656, JAPAN
***Department of Mechanical Engineering, The University of Tokyo
7-3-1 Hongo, Bunkyo-ku, Tokyo, 113-8656, JAPAN

The progress of microbubble flow simulations in our group is summarized. Numerical simulations of turbulent channel flows containing a lot of bubbles are performed for various Reynolds numbers. The skin friction increases at the lower Reynolds number of $Re_\tau \approx 200$, while it decreases at the higher Reynolds number of $Re_\tau \approx 1 \times 10^3$ which is same magnitude as that in typical experiments. These results are consistent with the dissipation theory, i.e., the reduction (or increase) of the total dissipation rate accounts for the drag reduction (or increase). Numerical simulations of homogeneous shear flows are also carried out in order to find the mechanism of reducing the turbulence production leading to the drag reduction. By investigating the distribution of vortical structures, the turbulence production tends to reduce when the turbulence introduced by the bubbles is small enough.

1 Introduction

Injecting microbubbles into a turbulent boundary layer is considered the most suitable for ships among several techniques proposed for reducing a skin friction, such as riblets, mechanical devices and polymers, because of high efficiency, low cost and no environmental contamination. Madavan *et al.* (1984) measured the skin friction on a plate placed in a water tunnel and reported an attractive result that the efficiency of the MicroBubble Drag Reduction (MBDR) reaches up to 80%. Although the MBDR has been studied over the last three decades since McCormick and Bhattachryya (1973) experimentally found this phenomenon, its mechanism is not fully understood yet. It is because the microbubbles obstruct detailed measurements.

It is very recent to overcome the difficulty in obtaining the detailed data on the flow modulation. With progresses in measurements and numerical simulations, the dynamic interaction between the bubble and liquid has enabled us to be locally captured and tells us helpful insight into the MBDR mechanism. On the numerical studies, we have simulated the microbubble flow since 2000 when the research project of *"Smart Control of Turbulence"* started. Although the numerical simulation seems appropriate for making clear the MBDR mechanism because of considering the local flow dynamics, it is not easy to reproduce the MBDR. Kawamura and Kodama (2002) and Sugiyama *et al.* (2002) simulated the channel turbulent flow containing deformable bubbles in the Front Tracking Method (FTM) generalized by Unverdi and Tryggvason (1992) and showed unsuccessful results that the skin friction increases with increasing void fraction. They set to the friction Reynolds number Re_τ less than 180, which is one or two orders of the magnitude smaller compared with typical experiments, due to computational restrictions. Sugiyama *et al.* (2002) also investigated the influences of other factors, such as the compressibility of bubble, and showed the increase of the skin friction. The first successful simulation to reproduce the MBDR was reported by Xu, Maxey and Karniadakis (2002). They employed the Force Coupling Method (FCM) developed by Maxey and Patel (2001). They simulated the turbulent channel flow at relatively low Reynolds number ($Re_\tau = 135$) with large bubbles ($d = 0.2h - 0.6h$, here d is the bubble diameter and h the channel half height h). They initially put bubbles in the layer near the wall and showed that the drag reduction transiently occurs when the bubbles disperse by turbulence. The authors also investigated the transient effects of the bubble concentration on the skin friction at the comparable Reynolds number in the Eulerian-Lagrangian Method (ELM), FTM and FCM (see Kodama *et al.*, 2003 and Sugiyama *et al.*,2003 & 2004). With respect to the fully resolved DNS for deformable bubbles, Lu , Fernández and Tryggvason (2004) recently investigated the deformation effect on the skin friction in the FTM. They showed that the deformable bubbles suppress forming quasi-streamwise vortices near the wall, which carry large Reynolds shear stress, and consequently the skin friction significantly reduces. Ferrante and Elghobashi (2004) performed point bubble simulations in the spatially developing turbulent boundary layer in the ELM. They showed that the non-zero divergence of the liquid velocity vector due to the inhomogeneous distribution of the void fraction causes the negative momentum transfer and displaces quasi-streamwise vortices away from the wall. Consequently, the MBDR rate reaches up to about 20% even at the small void fraction (α_0 =2%). Although the high efficiency of the MBDR in their result is attractive for the application, it is technically

difficult to generate the small bubble comparable to the wall unit with small energy input. Until now, although several different hypotheses for the MBDR have been proposed from the simulation results, the consensus on its mechanism is not reached yet.

In this paper, the progress of microbubble flow simulations for elucidating the drag reduction mechanism in our group is summarized. The simulation methods in the ELM, FCM and FTM for the microbubble flow in the channel are shown and flow modulations on the skin friction are discussed on the basis of the dissipation theory. Numerical simulations of homogeneous shear flows are also carried out in order to find the mechanism of reducing the turbulence production leading to the drag reduction.

2 Channel flow simulation with point bubbles

In order to investigate the effect of the large scale density fluctuation, point bubble simulations have been performed (Sugiyama *et al.*,2003). The purpose of this simulation is to examine the effects of the transient bubble dispersion (Xu *et al.*, 2001) and the velocity divergence (Ferrante and Elghobashi, 2004). The simulation code based on the Eulerian-Lagrangian Method (ELM, Murai and Matsumoto, 1996) is developed for the channel turbulent flow with microbubbles. In the ELM, the liquid phase is solved on the grid in the Eulerian way and the bubble is individually tracked in the Lagrangian way. The governing equations are based on the volume averaged equations for the mass and momentum conservations and discretized on grids much larger than the bubble diameter.

Governing equations consist of conservation equations of liquid and gas volume fraction,

$$\frac{\partial f_L}{\partial t} + \nabla \cdot (f_L \mathbf{u}_L) = 0, \quad \frac{\partial f_G}{\partial t} + \nabla \cdot (f_G \mathbf{u}_G) = 0, \tag{1}$$

and the momentum conservation equation for the liquid and gas mixture fluid,

$$\rho_L \left[\frac{\partial f_L \mathbf{u}_L}{\partial t} + \nabla \cdot (f_L \mathbf{u}_L \mathbf{u}_L) \right] = -\nabla p + \mu_L \nabla^2 \mathbf{u}_L, \tag{2}$$

where f is the volume fraction, t the time, $\mathbf{u}$ the velocity, p the pressure, μ the viscosity. The subscripts L and G represent liquid and gas phases, respectively. To close the set of equations, the constraints on the volume fraction $f_L + f_G = 1$ and the equation of translational motion of bubble taken the added inertia, steady drag force on the bubble and the liquid inertia around the bubble into account are used as constitutive equations. The fourth-order finite difference and second-order Adams-Bashforth methods are employed for the spatial and time derivatives, respectively. The interpolation from the liquid phase to the bubble centroid is approximated by using the fifth-order Lagrange's interpolation polynomial. The developing flow in a channel with a bubble injection from the top wall is simulated. The friction Reynolds number Re_τ is set to 150. The size of the simulation domain is set to $L_x \times L_y \times L_z = 10\pi h \times 2h \times \pi h$ divided by $N_x \times N_y \times N_z = 320 \times 64 \times 64$ grid points, in the streamwise (x), wall-normal (y) and spanwise (z) directions, respectively. The bubble diameter normalized by the wall unit d^+ is 2. The bulk void fraction f_{G0}, corresponding to the flow rate of the injected bubble divided by the total flow rate, is 0.3%. This f_{G0} is much smaller than in the typical experiments due to the numerical restriction.

Figure 1 shows a typical side view of an instantaneous bubble distribution. White points correspond to the bubbles. The bubbles are injected from $x = 0.5\pi h$ to πh with the vertical velocity of $-u_\tau$. As shown in Fig.1, the bubbles disperse by turbulence in the downstream.

Figure 2 shows the streamwise profile of C_f/C_{f0} on the top and bottom walls. C_f corresponds to the friction coefficient scaled by the inlet flow rate and the liquid density and C_{f0} to that in single phase flow. C_f is averaged over the time and in the spanwise direction. The skin friction on the top wall reduces at downstream of the injection when the bubble cluster disperses into the flow. This results seems to be consistent with that reported by Xu *et al.*(2001) in the force coupling method. The drag reduction persists to the outlet region at the distance from the end of the injection zone longer than $20h$, corresponding to 3000 wall units. Although the skin friction increases on the top and bottom walls near the bubble injection region, the total skin friction with bubbles becomes smaller than that in the singe phase flow.

In order to discuss the flow modulation, the Reynolds shear stress $-\bar{f}_L \overline{u_L v_L}$ is analyzed. This stress can be decomposed into

$$-\bar{f}_L \overline{u_L v_L} = \overbrace{-(\bar{f}_L \overline{u_L v_L} - \bar{f}_L \bar{u}_L \bar{v}_L)}^{\text{fluctuating component}} \underbrace{-\bar{f}_L \bar{u}_L \bar{v}_L}_{\text{mean component}}, \tag{3}$$

where the operator $\bar{\cdot}$ corresponds to averaging over the $xz-$plane. Note that the mean component is zero in the single phase flow because of $\bar{v}_L = 0$. The wall-normal profiles of the fluctuating and mean components

of the Reynolds shear stress on several x-positions are shown in Fig.3. The fluctuating component is almost independent of x, while the mean component is non-zero (i.e., $\bar{v}_L \neq 0$) and strongly dependent on x. That is the modulation of the turbulent flow is small, while that of the mean flow is large. It is caused by the velocity divergence effect due to the inhomogeneous distribution of the void fraction shown by Ferrante and Elghobashi (2004). We confirmed the drag reduction obtained in the ELM is caused by the velocity divergence effect from momentum balances. The results seem to be consistent with those reported by Xu *et al.*(2002) and Ferrante and Elghobashi (2004). In the ELM, however, the restriction of the bubble diameter being comparable to the wall unit is severe problem when considering the bubble diameter being $O(100)$ wall units in the typical experiments. In the following sections, the larger bubble will be treated in other simulation methods.

3 Channel flow simulations with finite size bubbles at low Reynolds number ($Re_\tau < 200$)

Extensive simulations of the channel turbulent flow have been performed at the friction Reynolds number Re_τ less than 200. So far, most of the microbubble flow simulations have also been performed at $Re_\tau \sim 150$ which is one or two orders of the magnitude smaller compared with typical experiments. Lu *et al.* (2004) showed both increase and reduction of the skin friction by examining the bubble deformation. For perfectly or nearly spherical bubbles in the low Reynolds number simulations, Xu *et al.*(2002) shows the drag reduction, while Kawamura and Kodama (2002) and Sugiyama *et al.* (2002& 2004) showed the drag increase in spite of almost same bubble size. In this section, we discuss this inconsistency and show what type of simulation method should be employed in elucidating the drag redution mechanism on the basis of the dissipation theory.

Xu *et al.*(2002) employed the Force Coupling Method (FCM). They assumed the bubble is spherical and rigid and neglected the buoyancy. In the FCM, the no-slip boundary condition is not fully satisfied on the bubble surface. Instead of the satisfaction of the boundary condition, the body force from the bubble to the liquid $\mathbf{F}_p$ is introduced in the momentum equation given by

$$\rho_L \frac{\mathrm{D}\mathbf{u}}{\mathrm{D}t} = -\nabla p + \mu_L \nabla^2 \mathbf{u} + \mathbf{F}_p. \tag{4}$$

Based on the Stokesian dynamics, $\mathbf{F}_p$ is expressed as,

$$F_{pi} = \sum_{l=1}^{N_b} \left(\underbrace{F_i^{(l)} \Delta(\mathbf{x} - \mathbf{Y}^{(l)}, \sigma_m)}_{\text{Force monopole}} + \underbrace{F_{ij}^{(l)} \frac{\partial}{\partial x_j} \Delta(\mathbf{x} - \mathbf{Y}^{(l)}, \sigma_d) \ldots}_{\text{Force dipole}} \right). \tag{5}$$

The force monopole is related to the translational motion of the bubble and equivalent to the reaction force against the drag force on the bubble. Xu *et al.*(2002) considered the force monopole. The force dipole is related to the velocity gradient around the bubble. Even if the bubbles perfectly follow the surrounding liquid, the force dipole is non-zero due to the shear flow. According to the Einstein's theory (Batchelor, 1967), the force dipole contributes to the increase of the skin friction. Although the method to include the force dipole in the FCM was generalized by Lomholt *et al.*(2002), Xu *et al.*(2002) neglected it. The authors developed the simple method to estimate the force dipole and showed reasonable result compared with the Einstein's theory (Sugiyama *et al.*, 2004).

The modulation of the skin friction will be discussed from the dissipation theory. In the single phase flow, the modulation of the skin friction is often discussed from the Reynolds shear stress or the production of the turbulent kinetic energy. The dissipation rate may seem the secondary effect because small eddies carrying large dissipation rate are generated as the result of the energy cascade from energy-containing large eddies. In the bubbly flow, however, the dissipation rate around the bubble locally changes due to the vorticity generation on the bubble surface. Based on Eq.4, total friction coefficient $C_f^{Top} + C_f^{Bot}$ in the channel flow is expressed as,

$$C_f^{Top} + C_f^{Bot} = \underbrace{\frac{8\mu_L h \langle \mathbf{S} : \mathbf{S} \rangle}{\rho_L \langle u \rangle^3}}_{\text{Dissipation}} + \underbrace{\frac{2h}{\langle u \rangle^3} \left[\frac{\mathrm{d}\langle \mathbf{u} \cdot \mathbf{u} \rangle}{\mathrm{d}t} - \frac{\mathrm{d}\langle u \rangle \langle u \rangle}{\mathrm{d}t} \right]}_{\text{Fluid motion}} \underbrace{- \frac{4h}{\rho_L \langle u \rangle^3} \langle \mathbf{u} \cdot \mathbf{F}_p \rangle}_{\text{Bubble force}}, \tag{6}$$

where $\mathbf{S}(= \{\nabla \mathbf{u} + (\nabla \mathbf{u})^T\}/2)$ is the strain rate tensor and the operator $\langle \cdot \rangle$ the volume averaging over the whole region. The effects of the buoyancy and the bubble deformation can be additionally included in Eq.6. The bubble force term in Eq.6 accounts for the bubble and liquid interaction. The third term in the RHS will temporally decrease if the transient effect, e.g. the large scale density change due to the bubble dispersion, is

important for the drag reduction. In the statistically steady situation, this term becomes negligible and the dissipation term dominant.

The effect of non-uniform distribution of the initial bubble position on the skin friction is investigated under a similar condition to the computation reported by Xu *et al.* (2002). Before introducing the bubbles, a fully developed single-phase turbulent channel flow at $Re_\tau = 150$ is computed. The size of the simulation domain is set to $L_x \times L_y \times L_z = 2\pi h \times 2h \times \pi h$ divided by $N_x \times N_y \times N_z = 64 \times 64 \times 64$ grid points. The periodic boundary condition is imposed in x and z directions. The bubble radius a and the bubble number N_b are set to $0.25h$ and 30, respectively. The initial bubble location is the layer near the top wall.

The temporal evolution of the total friction coefficient $C_f^{Top} + C_f^{Bot}$ and the dissipation term in Eq.6 are shown in Fig.4. $C_f^{Top} + C_f^{Bot}$ is strongly dependent on the dissipation term. When neglecting the force dipole, the fluid motion term in Eq.6 initially decreases due to the transient density change caused by the bubble dispersion. The decrease of the fluid motion term transfers to the decrease of the dissipation term as the flow evolves. On the other hand, when considering the force dipole, the dissipation around the bubble becomes large due to the shear flow modulation.

The skin friction is likely to increase due to the force dipole. In the force coupling simulation, however, the local no-slip boundary condition is not fully satisfied on the bubble surface even if the force dipole is introduced and the steady Stokes dynamics is assumed for the two-phase interaction even at the finite Reynolds number. The direct simulations, where the boundary condition is locally approximated, are also performed under the almost same condition. We simulated the flows containing the rigid bubble with the no-slip boundary based on the method proposed by Sugiyama *et al.* (2001) or the deformable bubble with the free slip one using the code developed by Kawamura and Kodama (2002). Then, similarly to the force coupling simulation with the force dipole, we confirmed the drag increase in both simulations due to the local increase of the dissipation rate around the bubble. For example, Fig.5 shows that a conditionally sampled $(\mathbf{S} : \mathbf{S})^*$ for the DNS with the rigid bubble with respect to the nearest length from the bubble centroid λ. Here, $(\mathbf{S} : \mathbf{S})^*$ corresponds to the deviation of the $\mathbf{S} : \mathbf{S}$ from that averaged over the $xz-$plane. As shown in Fig.5, the $(\mathbf{S} : \mathbf{S})^*$ is likely to increase near the bubble surface ($\lambda/a > 1$). The positive change of $(\mathbf{S} : \mathbf{S})^*$ contributes to the increase of the skin friction as expected by Eq.6. So far, we confirmed that the inertial terms in Eq.6 can contribute to the drag reduction but the increase of the dissipation term is larger than the decrease of the inertial terms.

The drag increase result shown in this section is reasonable in view of the dissipation theory. The present simulation condition is rather limited so that we cannot conclude if the drag reduction occurs at the low Reynolds number. However, we can say that the simulation method resolving the dissipation rate near the bubble surface should be chosen in investing the skin friction change.

4 Channel flow simulations at high Reynolds number comparable to that in typical experiment ($Re_\tau \sim 1000$)

In the last year, the authors reported the Large Eddy Simulation (LES) at the high Reynolds number ($Re_\tau = 1100$) comparable to that in the experiment by Moriguchi and Kato (2002) (see Sugiyama *et al.*,2004). The result showed that both the skin friction and the total dissipation rate transiently reduce during a short period ($t^+ \leq 480$). Until now, we have simulated up to $t^+ = 1800$. In this section, the several statistical data are discussed.

The numerical method used in this study is based on the Front-Tracking Method (FTM) to deal with the deformable bubble (Kawamura and Kodama, 2002). In order to determine the simulation condition, the experiment by Moriguchi and Kato (2002) is referred. The dimensionless parameters are Re_τ=1,100, d/h=0.2, the Froude number $F_d = U_m/\sqrt{gh} = 16$, and the Weber number $We = \rho U_m^2 d/\sigma = 34$. The size of the simulation domain is set to $L_x \times L_y \times L_z = 6.4h \times 2h \times 3.2h$ divided by $N_x \times N_y \times N_z = 256 \times 128 \times 128$ grid points. Initially, 98 bubbles are introduced and the length between the bubble centroid and the wall is set to $0.2h$. In balance with the buoyancy and bubble dispersion effects, the bubbles are likely to locate near the top wall.

The instantaneous distribution of the bubble near the wall at $t^+ = 1800$ is shown in Fig.6. The color contour indicates the magnitude of the streamwise velocity. The bubble diameter is 220 wall units. Although seemingly the bubble is very close to the wall, the nearest bubble surface from the wall is located at the buffer layer or the log-law region. Thus, most of the bubble body is included in the outer layer ($y^+ > 50$).

The temporal evolution of the relative friction coefficient C_f/C_{f0} on the top wall is shown in Fig.7. The tendency of $C_f/C_{f0} < 1$ indicates that the skin friction reduces on the top wall. The relation between C_f/C_{f0} and the void fraction is shown in Fig.8. The symbols $\bullet$ and $+$ correspond to the results in the present simulation and in the experiment by Moriguchi and Kato (2002), respectively. As shown in Fig.8, the

magnitude of the drag reduction in the present simulation shows good agreement with that in the experiment within the measurement error.

The mean velocity profiles at $Re_\tau = 1100$ and 180 are shown in Figs.9 and 10, respectively. The velocity is normalized by the friction velocity u_τ so that the increase of the normalized velocity accounts for the drag reduction. The bottom figure shows the change of the liquid velocity by adding the bubble. As shown in Fig.9 in the higher Reynolds number case, the mean velocity increases in the region of $y^+ > 200$, contributing to the drag reduction. On the other hand, the mean velocity decreases in the near wall region $y^+ < 100$ where the mean velocity gradient is large. It is seen from Fig.10 in the lower Reynolds number case that the mean velocity decreases in almost whole region. This result is consistent with the drag increase obtained at the lower Reynolds number. Note that the center of the channel corresponds to $y^+ = Re_\tau$. Thus, the velocity increase in the outer region is likely to occur at the high Reynolds number. On the velocity modulation, we also confirmed a consistent result with the optical measurement by Kitagawa *et al.*(2004) that the Reynolds shear stress $-\overline{u'v'}$ of the bubble is considerably smaller than that of the liquid phase.

The time histories of the relative dissipation rate $\langle\overline{\mathbf{S}:\mathbf{S}}\rangle_L$ at $Re_\tau = 180$ and $Re_\tau = 1100$ are shown in Fig.11. The dissipation rate at the lower Reynolds number increases by adding the bubble leading to the drag increase. On the other hand, the dissipation rate at the higher Reynolds number decreases leading to the drag reduction. The decrease magnitude of the total dissipation rate is rather smaller than the that of the skin friction on the top wall shown in Fig.7. It is because the total dissipation rate contributes to the skin frictions not only on the top wall but also on the bottom one. We confirmed that the sum of the friction coefficients on the top and bottom walls is well correlated to the total dissipation rate.

As shown in Fig.5, the local increase of the dissipation rate around the bubble leading to the drag increase can be found at the low Reynolds number. Although the flow modulation is checked from the data at the high Reynolds number, the locally characteristic structure to reduce the dissipation rate cannot be found around the bubble. This result may suggest that the global turbulence modulation through the production and dissipation process for the turbulent kinetic energy is more important than the local flow modulation around the bubbles. In the next section, the turbulence production mechanism by the presence of the bubbles is investigated by simulating the homogeneous shear flow.

5 Homogeneous shear flow simulation

Although the drag reduction mechanism is not fully made clear yet, it is presumed that the Reynolds number is important parameter and the turbulence seems to be globally modulated. On the turbulence effect, Fukagata *et al.* (2002) quantified the contribution of the Reynolds shear stress to the skin friction. Based on their theory, we pay attention to the turbulence production expressed by the product of the Reynolds shear stress and the mean shear. We consider $x-$component of the averaged momentum equation based on Eq.4 given by

$$\rho_L\left[\frac{\partial\bar{u}}{\partial t}+\frac{\partial\overline{u'v'}}{\partial y}\right]=\left(-\frac{\mathrm{d}P}{\mathrm{d}x}\right)+\mu_L\frac{\partial^2\bar{u}}{\partial y^2}+\bar{F}_{px}, \tag{7}$$

where the operator $\bar{\cdot}$ corresponds to averaging over the $xz-$plane and $\overline{f'g'}=\overline{fg}-\bar{f}\bar{g}$. Eq.6 can be decomposed into

$$\frac{\rho_L\langle\bar{u}\rangle^3(C_f^{Top}+C_f^{Bot})}{4h}=\mathcal{P}+\mu_L\left\langle\left(\frac{\partial\bar{u}}{\partial y}\right)^2\right\rangle+\frac{\rho_L}{2}\left[\frac{\mathrm{d}\langle\bar{\mathbf{u}}\cdot\bar{\mathbf{u}}\rangle}{\mathrm{d}t}-\frac{\mathrm{d}\langle\bar{u}\rangle\langle\bar{u}\rangle}{\mathrm{d}t}\right]-\langle\bar{\mathbf{u}}\cdot\bar{\mathbf{F}}_p\rangle, \tag{8}$$

$$\mathcal{P}=2\mu_L\langle\overline{\mathbf{S}':\mathbf{S}'}\rangle+\frac{\rho_L}{2}\frac{\mathrm{d}\langle\overline{\mathbf{u}'\cdot\mathbf{u}'}\rangle}{\mathrm{d}t}-\langle\overline{\mathbf{u}'\cdot\mathbf{F}'_p}\rangle, \tag{9}$$

where the turbulence production $\mathcal{P}$ is given by

$$\mathcal{P}=-\rho_L\left\langle\overline{u'v'}\frac{\partial\bar{u}}{\partial y}\right\rangle. \tag{10}$$

In the RHS of Eq.8, the term containing the fluctuating velocity is only the first one. Thus, $\mathcal{P}$ is considered to account for the contribution of the turbulence eddy to the skin friction.

In order to clarify the mechanisms of the drag reduction, it is useful to quantify the influence of parameters by means of the DNS. However, the simulation of the channel flow containing bubbles requires a lot of computational time so that this flow is not appropriate for the parametric study. In this section, the homogeneous turbulent shear flow with uniform shear and no solid boundary is simulated instead of the channel flow. This flow is considered the simplest flow to appropriately investigate the vortical structure generating the Reynolds

shear stress. The modulation of the turbulence production $\mathcal{P}$, which is significant for the skin friction (Eq.8), is discussed by estimating $\mathcal{P}$ based on Eq.9 for the fluctuating velocity field.

The DNS of the bubbly flow is performed based on the method proposed by Kajishima *et al.*(2001) for the rigid bubble or in the FTM for the deformable bubble. Governing equations for fluctuating velocity u_i and pressure p consist of the mass and momentum conservation equation. In the tensor form, these normalized equations for the rigid bubble flow are given by

$$\frac{\partial u_i}{\partial x_i} = 0, \tag{11}$$

$$\frac{\partial u_i}{\partial t} + U_1 \frac{\partial u_i}{\partial x_1} + S\delta_{i1}u_2 + u_j \frac{\partial u_i}{\partial x_j} = \frac{\partial}{\partial x_j}\left(-p\delta_{ij} + 2\nu S_{ij}\right) + F_{pi}, \tag{12}$$

where $S(= \mathrm{d}U_1/\mathrm{d}x_2)$ is the shear rate and $U_1 = (S(x_2 - L_2/2), 0, 0)$ is the mean velocity. S is set to 1. The size of the simulation domain is set to $L_1 \times L_2 \times L_3 = 1 \times 1 \times 1$ divided by $N_1 \times N_2 \times N_3 = 64 \times 64 \times 64$ or $128 \times 128 \times 128$ grid points, in the streamwise (x_1), vertical (x_2) and spanwise (x_3) directions, respectively. There is no wall in the flow, thus the periodic boundary condition is imposed in the x_1 and x_3 directions and the shear-periodic boundary condition (Gerz *et al.*,1989) in the x_2 direction. Initial turbulence field is randomly given by the solenoidal velocity vector satisfying the prescribed three-dimensional energy spectrum $\tilde{E}(k)$ shown by Gerz *et al.*(1989). Simulation parameters consist of the shear Reynolds number $Re(= Sd^2/\nu)$, the initial root-mean-square (rms) of fluctuating velocity $u_{\mathrm{rms}0}$ and the Weber number $We(= \rho_L S^2 d^3/\sigma)$ (only for the deformable bubble). In both Re and We, Sd is used as the velocity scale. In order to determine the simulation condition, the parameters in the previous experiments performed by Moriguchi and Kato (2002) and Oishi *et al.*(2003) are referred. The ranges of Re and $u_{\mathrm{rms}0}$ are $581 - 2326$ and $0.411 - 6.576$, respectively. We is set to 5.0 or 11.5. The bubble diameter d and the number of bubbles N_b are set to 0.2 and 8, respectively. Correspondingly, the void fraction α_0 is 3.35%. Initially, the simulation domain is divided into 8 cubic boxes and the bubble centroids are located at the center of these boxes. The time derivative of the turbulent kinetic energy $E(= \langle u_i u_i/2 \rangle)$ for the rigid bubble flow is expressed as,

$$\frac{\mathrm{d}E}{\mathrm{d}t} = \mathcal{P} - \epsilon + \langle F_{pi} u_i \rangle, \tag{13}$$

where $\mathcal{P}(= -S\langle u_1 u_2 \rangle)$ is the turbulence production and $\epsilon(= 2\nu\langle S_{ij} S_{ij} \rangle)$ the turbulence dissipation. The last term in the RHS of Eq.13 corresponds to the contribution of the bubble with no-slip boundary. In the fully developed state, the growth of E, $\mathcal{P}$ and ϵ is exponential in time. Scaled turbulence production $\mathcal{P}/E$ is discussed.

$\mathcal{P}/E$ is shown in Fig.12. $Re_t(= u_{\mathrm{rms}} d/\nu)$ in Fig.12 corresponds to the turbulence Reynolds number, here $u_{\mathrm{rms}}(= \sqrt{2E/3})$ is the rms velocity. Re_t is used for the horizontal axis in order to make equitable comparison under the same E. As shown in Figs.12(a)- 12(d), the turbulence production $\mathcal{P}/E$ tends to increase by adding the bubbles at the lower Reynolds number ($Re = 581$), while $\mathcal{P}/E$ to reduces at the higher Reynolds number ($Re = 2326$) in both flows containing deformable and rigid bubbles. From Eq.8, the reduction (or increase) of $\mathcal{P}/E$ contributes to the drag reduction (or increase) in the channel flow due to the fluctuating velocity. The reduction of $\mathcal{P}/E$ in the higher Reynolds number (i.e., the lower viscosity) seems consistent with the drag reduction shown in §4. It is seen from Figs.12(d) and 12(e) that $\mathcal{P}/E$ tends to increase by adding the bubbles in the smaller $u_{\mathrm{rms}0}$ case, though $\mathcal{P}/E$ to reduce in the larger $u_{\mathrm{rms}0}$ case even at the same Re. As recognized from the horizontal axis, Re_t in the smaller $u_{\mathrm{rms}0}$ case (Fig.12(e)) is much lower than that in the larger $u_{\mathrm{rms}0}$ case (Fig.12(d)). This result indicates that the turbulence intensity is also important parameter for distinguishing reduction and increase of the skin friction.

In order to grasp the flow structure when the turbulence production reduces or increases, the vortical structure is visualized. In the present study, the vortex is educed by means of a λ_2-definition proposed by Jeong and Hussain (1995). λ_2 corresponds to the second largest eigenvalue of a tensor $S_{ik}S_{kj} + \Omega_{ik}\Omega_{kj}$, here $\Omega_{ij} = (\partial u_i/\partial x_j - \partial u_j/\partial x_i)/2$. If $\lambda_2 < 0$, the swirling motion may exceed the straining motion. In order to educe the vortical structure objectively, λ_2 is scaled by u_{rms} and the Kolmogorov length scale η based on the numerical investigation by Tanahashi *et al.*(2001), who identified the fine scale eddy by using II (corresponding to the second invariant of the velocity gradienttensor). Incidentally, Iida *et al.*(2000) educed the vortical structures in the homogeneous shear flow by both the λ_2- and II-definitions with prescribed thresholds and showed there was no difference in the definitions.

The side view of the typical vortical structure visualized by isosurface of $\lambda_2/(u_{\mathrm{rms}}/\eta)^2 = -0.02$ is shown in Fig.13. The cyan and yellow surfaces correspond to $\omega_1 > 0$ and $\omega_1 < 0$, respectively. As shown in Figs.13(A) and 13(C), corresponding to the cases in which the bubbles increase the turbulence production (Figs.12(c) and 12(e)), potent eddies preferentially exist around bubbles. The elongated structures seem slightly to incline

from the x_1-direction towards the x_2-direction. Such an inclination of the vortical structure generates the negative correlation between u_1 and u_2, contributing to the positive turbulence production. According to Adrian and Moin (1988) and Kida and Tanaka (1992), the Reynolds shear stress (i.e., $\mathcal{P}$) is likely to take large value between pairs of counter rotating vortices. In Figs.13(A(b)) and 13(C(b)), the counter rotating vortices, as drawn by different colors, are observed near the bubble. Indeed, we confirmed the preferentially organized vortices contain quite large Reynolds shear stresses from the conditional sampling. The case of Fig.13(B) corresponds to that in which the bubbles decrease the turbulence production (Fig.12(d)). The integral length l is equivalent to that in Fig.13(C(b)), corresponding to $l = 0.23$. Unlike the cases at the lower Re (Fig.13(A(b))) and the smaller $u_{\rm rms0}$ (Fig.13(C(b))), it is seen from Fig.13(B(b)) that the preferentially potent eddies do not clearly observed around the bubble. The uniform distribution of the eddies indicates the Reynolds shear stress is also uniformly distributed. Indeed, we confirmed that the x_2-position of the bubble and $-\overline{u_1u_2}$, corresponding to the Reynolds stress averaged over x_1x_3-plane, are not well correlated. So far, we also performed computatitions based on the linear theory, corresponding to the rapid distortion theory (Lee *et al.*, 1990), and confirmed that the nonlinear interaction among the small scale motion is essential for reducing the turbulence production. Moreover, the small scale motion to generate the Reynolds shear stress is considerably suppressed by the bubble containing no turbulence eddy when $\mathcal{P}/E$ reduces. From results of the uniform profile of $-\overline{u_1u_2}$ in the liquid phase and the suppression of $-u_1u_2$ inside the bubble, the reduction of $\mathcal{P}/E$ by adding the bubble is considered to be caused by decreasing the degree of freedom of the turbulence motion.

The scaled production ratio $\langle\mathcal{P}/E\rangle/\langle(\mathcal{P}/E)_0\rangle$ is shown in Fig.14, here $\langle(\mathcal{P}/E)_0\rangle$ is for the single phase flow. From Figs.14(a) and 14(b), $\langle\mathcal{P}/E\rangle/\langle(\mathcal{P}/E)_0\rangle$ becomes smaller at the higher shear and turbulence Reynolds numbers. The result of $\langle\mathcal{P}/E\rangle/\langle(\mathcal{P}/E)_0\rangle > 1$ at the lower Reynolds numbers is caused by the preferentially organized vortices around the bubble as shown in Figs.13(A) and 13(C). The dotted line corresponds to the liquid volume fraction. Although the number of data is small, $\langle\mathcal{P}/E\rangle/\langle(\mathcal{P}/E)_0\rangle$ seems to approach the liquid volume fraction at the higher Reynolds numbers. This result supports the hypothesis that the reduction of $\mathcal{P}/E$ is caused by decreasing the degree of freedom of the turbulence motion if the turbulence introduced by the bubble is small enough. Fig.14(c) shows the influence of the bubble deformation with different Weber numbers ($We = 5.0$, 11.5). At the lowest Reynolds number, $\langle\mathcal{P}/E\rangle$ increases in both cases of $We = 5.0$ and 11.5 by adding the bubble. The increase ratio is considerably smaller at the higher Weber number. This result indicates that the deformation of bubbles suppresses the turbulence production. On the other hand, $\langle\mathcal{P}/E\rangle$ reduces at the higher Reynolds number in both Weber number cases. Unlike the cases at the lower Reynolds number, the influence of the Weber number is quite small on the decrease ratio of $\langle\mathcal{P}/E\rangle$. For the deformable bubble flow, $\langle\mathcal{P}/E\rangle/\langle(\mathcal{P}/E)_0\rangle$ also seems to approach the liquid volume fraction.

6 Conclusions

The progress of microbubble flow simulations for elucidating the drag reduction mechanism in our group is summarized. By using several simulation techniques such as the Eulerian-Lagrangian method, force coupling one and front tracking one, the following results are obtained.

- In a transient process of developing flows, the bubble dispersion contributes to the drag reduction, while the increase of the local velocity gradient around the bubble contributes to the drag increase. Although the latter effect requires a lot of computational resources, it should be considered when investigating the drag reduction mechanism.

- In the low Reynolds number turbulence ($Re_\tau < 200$), the increase of the dissipation rate by the presence of bubbles cannot be negligible so that the skin friction consequently tends to increase.

- At the friction Reynolds number higher than about 1000, the turbulence structure is globally modulated to reduce the skin friction by the bubble motion. In the large eddy simulation at the friction Reynolds number of $Re_\tau = 1100$ and the void fraction of 1%, the skin friction reduces in $2-3$% as a result of reducing the total dissipation rate. The drag reduction magnitude is comparable to the experimental result obtained by Moriguchi and Kato(2002) within a measurement error.

- From the homogeneous shear flow simulation, the Reynolds shear stress increases by adding the bubble when potent eddies are preferentially generated around bubbles, while it reduces when the bulk turbulence is large enough. When shear and turbulence Reynolds numbers and Weber number are large, the Reynolds shear stress tends to be smaller, which may lead to the drag reduction.

References

Adrian, R.J. and Moin, P. (1988) Stochastic estimation of organized turbulent structure: homogeneous shear flow, *J. Fluid Mech.*, **190**, 531-559.

Batchelor, G.K. (1967) *'An Introduction to Fluid Dynamics,'* Chap. 4, Cambridge University Press.

Ferrante, A. and Elghobashi, S., (2004) On the physical mechanisms of drag reduction in a spatially-developing turbulent boundary layer laden with microbubbles, *J. Fluid Mech.*, **503**, 345-355.

Gerz, T., Schumann, U. and Elghobashi, S.E. (1989) Direct simulation of stably stratified homogeneous turbulent shear flows, *J. Fluid Mech.*, **200**, 563-594.

Hinze, J.O. (1975) *'Turbulence,'* (2nd edition), Sec.5-7, McGraw-Hill.

Iida, O, Iwatsuki, M. and Nagano, Y. (2000) Vortical turbulence structure and transport mechanism in a homogeneous shear flow, *Phys. Fluids*, **12**, 2895-2905.

Jeong, J. and Hussain, F. (1995) On the identification of a vortex, *J. Fluid Mech.*, bf 285, 69-94.

Kajishima, T., Takiguchi, S., Hamasaki, H. and Miyake, Y. (2001) Turbulence structure of particle-laden flow in a vertical plane channel due to vortex shedding, *JSME Int. J.* Ser. B, **44**, 526-535.

Kawamura, T. and Kodama, Y. (2002) Numerical simulation method to resolve interactions between bubbles and turbulence, *Int. J. Heat and Fluid Flow*, **23**, 627-638.

Kida, A. and Tanaka, M. (1992) Reynolds stress and vortical structure in a uniformly sheared turbulence, *J. Phys. Soc. Japan*, **61**, 4400-4417.

Kitagawa, A., Hishida, K. and Kodama, Y. (2004) Two-phase turbulence structure in a microbubble channel flow, *Proc. of 5th Symp. on Smart Control of Turbulence*, (The Univ. of Tokyo, Tokyo, Japan), 135-144.

Lee, M.J., Kim, J. and Moin, P., (1990) Structure of turbulence at high shear rate, *J. Fluid Mech.*, **216**, 561-583.

Lomholt, S, Stenum, B. and Maxey, M.R., (2002) Experimental verification of the force coupling method for particulate flows, Int. J. Multiphase Flow, 28, 225.246.

Lu, J., Fernández, A. and Tryggvason, G., (2004) The effect of bubbles on the wall shear in a turbulent channel flow, *Phys. Fluids* (submitted).

Madavan, N.K., Deutsch, S. and Merkle, C.L. (1984) Reduction of turbulent skin friction by microbubbles, *Phys. Fluids*, **27**, 356-363.

Maxey, M.R. and Patel, B.K. (2001) Localized force representations for particles sedimenting in Stokes flow, *Int. J. Multiphase Flow*, **27**, 1603-1626.

McCormick, M.E. and Bhattacharyya, R. (1973) Drag reduction of a submersible hull by electrolysis, *Naval Engineers J.*, **85**, 11-16.

Moriguchi, Y., and Kato, H. (2002), Influence of microbubble diameter and distribution on frictional resistance reduction, *J. Mar. Sci. Technol.*, **7**, 79-85.

Murai, Y. and Matsumoto, Y. (1996) Numerical simulation of turbulent bubbly plumes using Eulerian-Lagrangian bubbly flow model equations, *Proc. of ASME FED*, FED**236**, 67-74.

Oishi, Y., Murai, Y., Ishikawa, M. and Yamamoto, F., (2003) PTV measurement of near-wall bubbly flow in a horizontal channel, *Proc. of Fluid Engineering Conference 2003, Japan Society of Mechanical Engineers*, 1302 (CD-ROM, in Japanese).

Sugiyama, K., Kawamura, T., Takagi, S. and Matsumoto, Y. (2002) Numerical simulation on drag reduction mechanism by microbubbles, *Proc. of 3rd Symp. on Smart Control of Turbulence*, (The Univ. of Tokyo, Tokyo, Japan), 129-138.

Sugiyama, K., Kawamura, T., Takagi, S. and Matsumoto, Y. (2003) Numerical simulation of transient microbubble flow, *Proc. of 4th Symp. on Smart Control of Turbulence*, (The Univ. of Tokyo, Tokyo, Japan), 51-60.

Sugiyama, K., Kawamura, T., Takagi, S. and Matsumoto, Y. (2004) The Reynolds number effect on the microbubble drag reduction, *Proc. of 5th Symp. on Smart Control of Turbulence*, (The Univ. of Tokyo, Tokyo, Japan), 31-43.

Sugiyama, K., Takagi, S. and Matsumoto, Y. (2001) Multi-Scale analysis of bubbly flows, *Computer Methods in Applied Mechanics and Engineering*, **101**, 689-704.

Tanahashi, M., Iwase, S. and Miyauchi, T. (2001) Appearance and alignment with strain rate of coherent fine scale eddies in turbulent mixing layer, *J. of Turbulence*, **2**, No. 006.

Unverdi, S.O. and Tryggvason, G. (1992) A front-tracking method for viscous, incompressible, multi-fluid flows, *J. Comput. Phys.*, **100**, 25-37.

Xu, J., Maxey, M.R. and Karniadakis, G.E. (2002) DNS of turbulent drag reduction using micro-bubbles, *J. Fluid Mech.* **468**, 271-281.

Figure 1: Visualization of computed flow in the point bubble simulation (ELM)

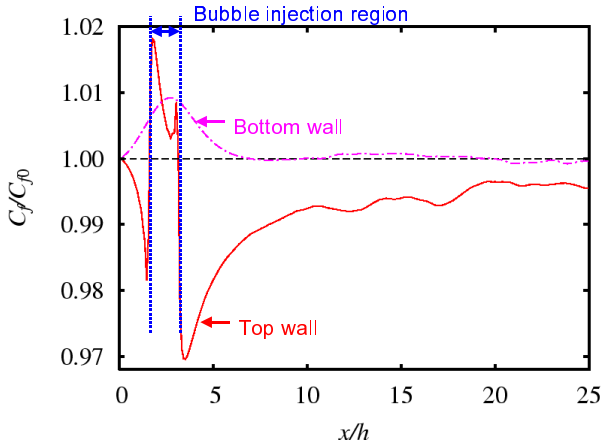

Figure 2: Streamwise distribution of skin friction ratio on top and bottom walls in the ELM

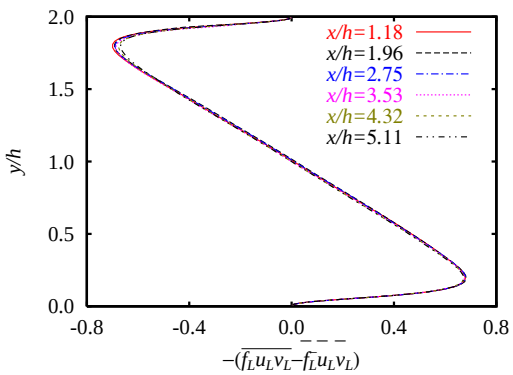

(a) Fluctuating component

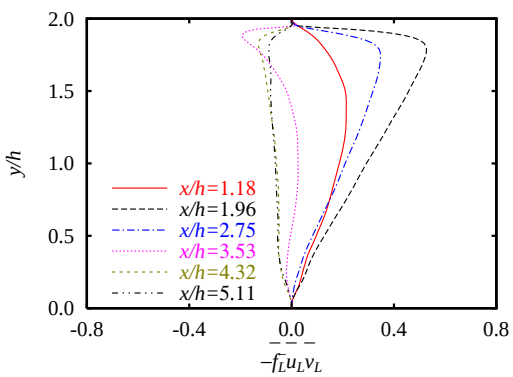

(b) Mean component

Figure 3: Wall-normal distributions of the fluctuating and mean components of the Reynolds shear stress in the ELM ($-\bar{f}_L\overline{u_L v_L}$) on x/h=1.18, 1.96, 2.75, 3.53, 4.32 and 5.11.

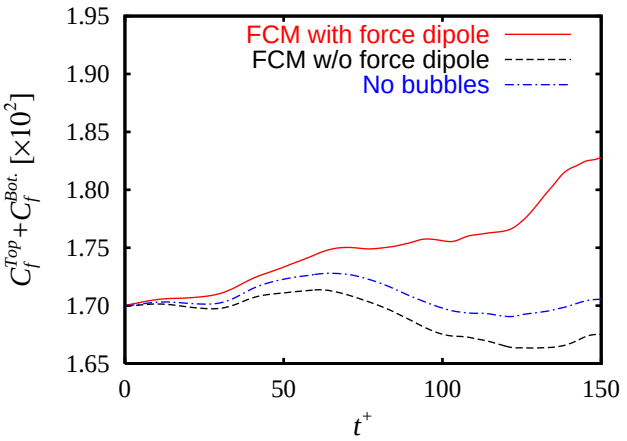

(a) $C_f^{Top} + C_f^{Bot.}$

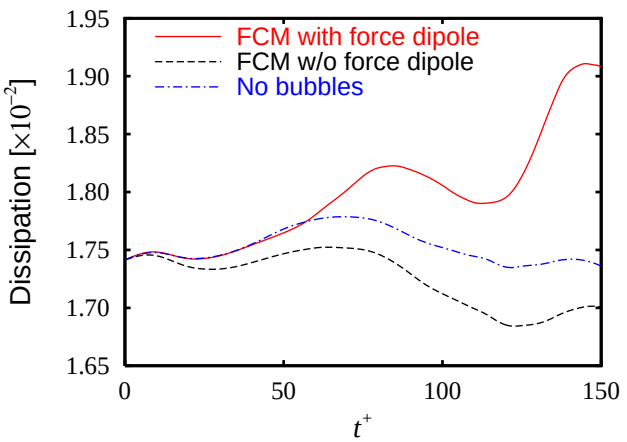

(b) Dissipation term of Eq.6

Figure 4: Temporal evolution of the total friction coefficient and the energy dissipation at $Re_\tau = 150$ in the FCM

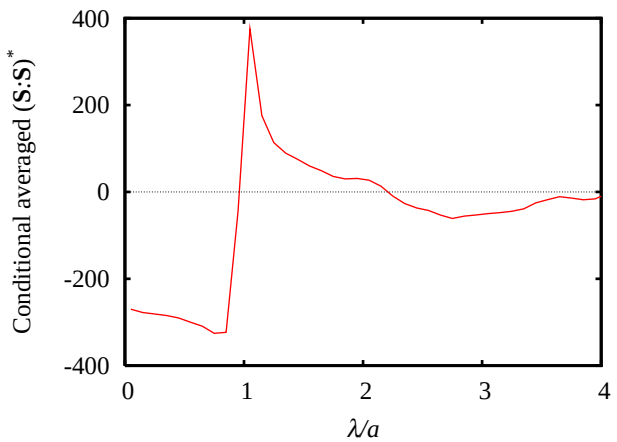

Figure 5: Conditionally averaged $(\mathbf{S} : \mathbf{S})^*$ with respect to the nearest length from bubble λ at $Re_\tau = 150$ in the DNS

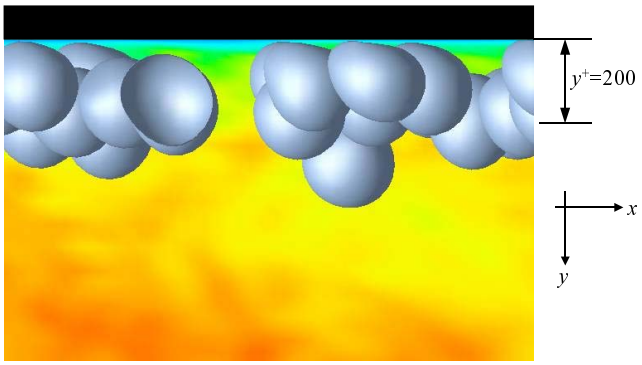

Figure 6: Distribution of bubbles near the wall at $Re_\tau = 1100$

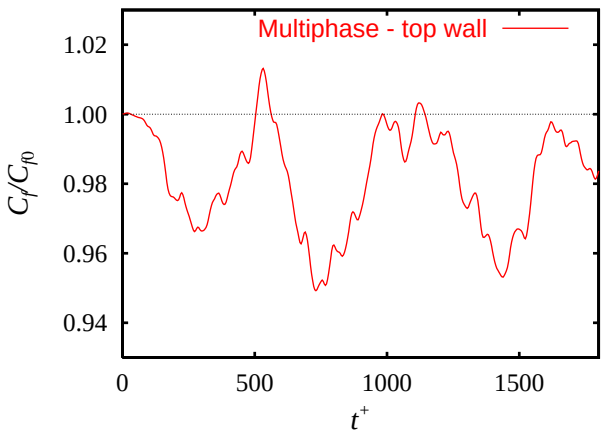

Figure 7: Temporal evolution of the relative friction coefficient on the top wall at $Re_\tau = 1100$

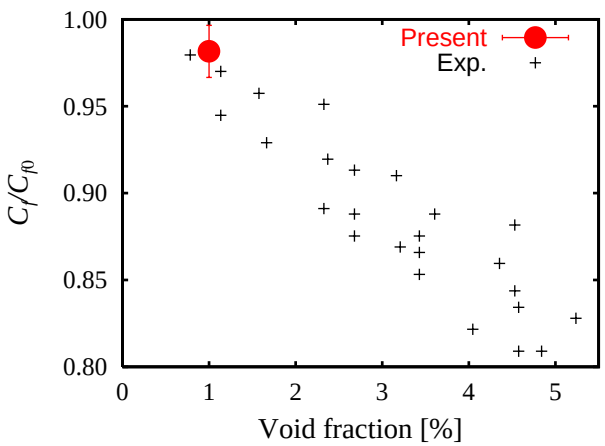

Figure 8: Relative friction coefficient vs. void fraction at $Re_\tau = 1100$ (•: Present; +: Moriguchi and Kato, 2002)

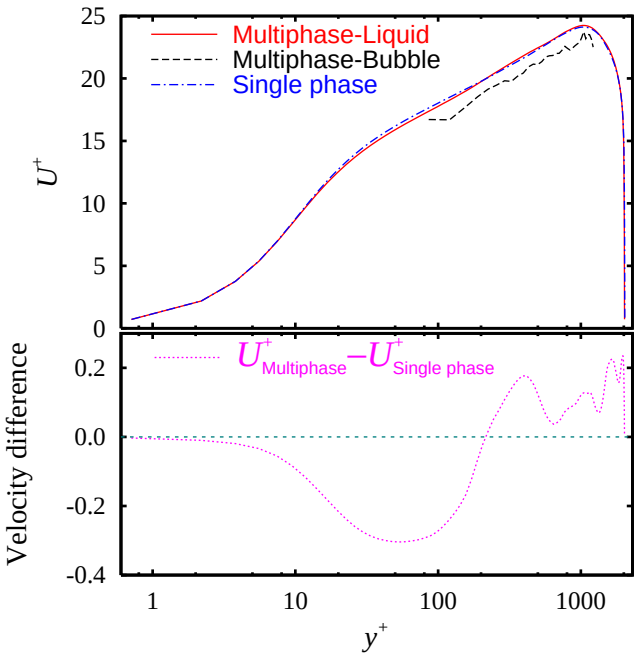

Figure 9: Mean velocity profile at $Re_\tau = 1100$

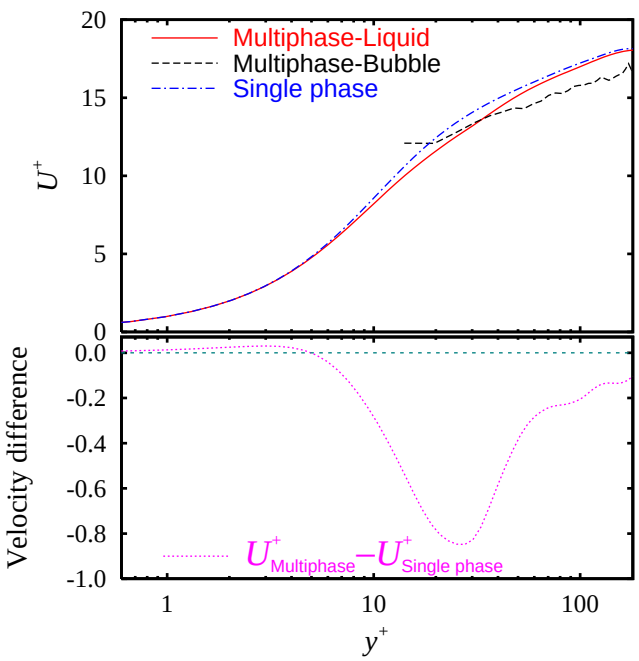

Figure 10: Mean velocity profile at $Re_\tau = 180$

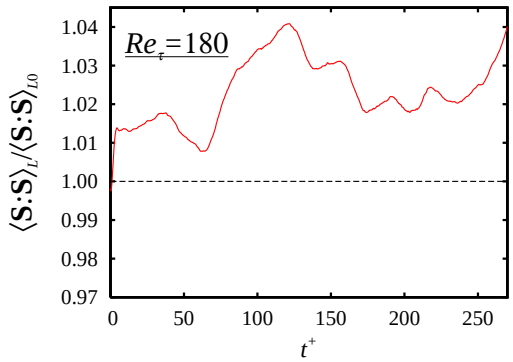

(a) $Re_\tau = 180$

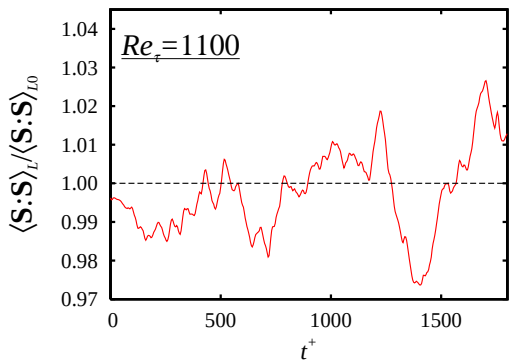

(a) $Re_\tau = 1100$

Figure 11: Time history of the total dissipation rate with deformable bubbles

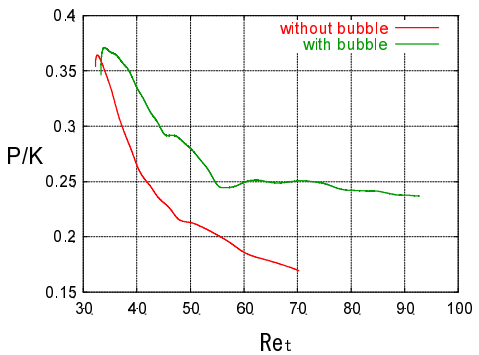

(a) $Re = 581$, $We = 5.0$, $u_{\mathrm{rms}0} = 1.644 \times 10^{-2}$ (deformable bubble)

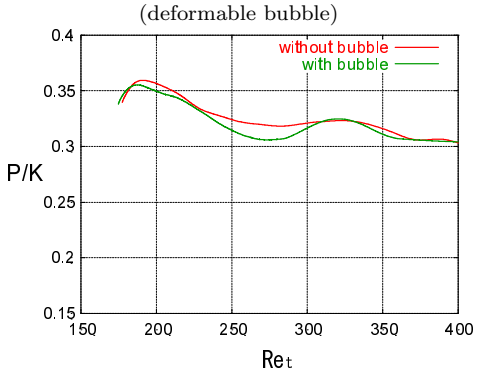

(b) $Re = 2326$, $We = 11.5$, $u_{\mathrm{rms}0} = 1.644 \times 10^{-2}$ (deformable bubble)

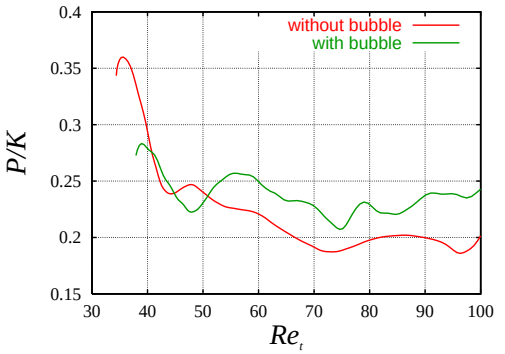

(c) $Re = 581$, $u_{\mathrm{rms}0} = 1.644 \times 10^{-2}$ (rigid bubble)

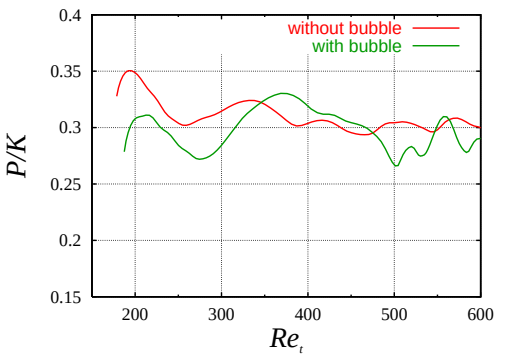

(d) $Re = 2326$, $u_{\mathrm{rms}0} = 1.644 \times 10^{-2}$ (rigid bubble)

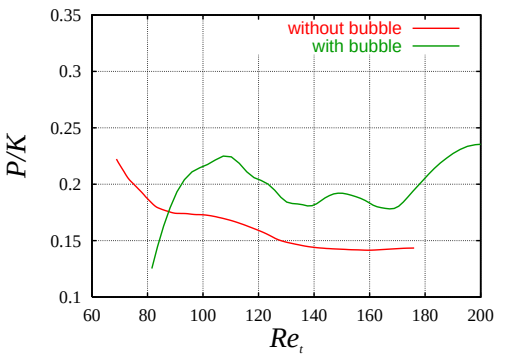

(e) $Re = 2326$, $u_{\mathrm{rms}0} = 0.411 \times 10^{-2}$ (rigid bubble)

Figure 12: Scaled production $\mathcal{P}/E$ vs. turbulent Reynolds number Re_t

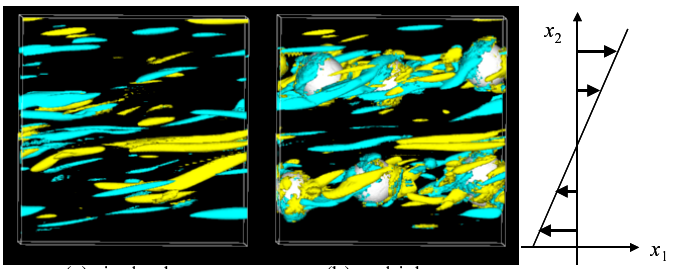

(a) single phase (b) multiphase

(A) $Re = 581$, $u_{\mathrm{rms}0} = 1.644 \times 10^{-2}$, $t = 10$

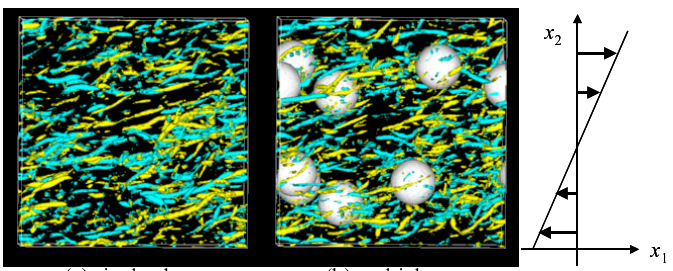

(a) single phase (b) multiphase

(B) $Re = 2326$, $u_{\mathrm{rms}0} = 1.644 \times 10^{-2}$, $t = 9.2$

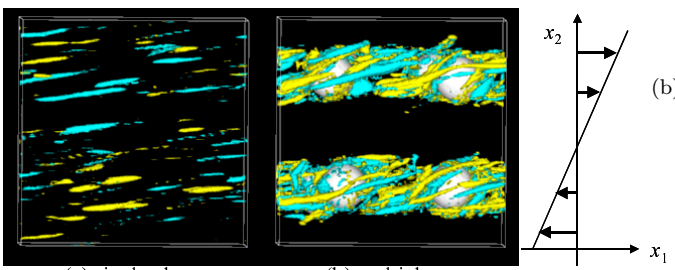

(a) single phase (b) multiphase

(C) $Re = 2326$, $u_{\mathrm{rms}0} = 0.411 \times 10^{-2}$, $t = 10$

Figure 13: Distribution of vortical structure visualized by using isosurfaces of λ_2 corresponding to the second largest eigenvalue of $S_{ik}S_{kj}+\Omega_{ik}\Omega_{kj}$ $(\lambda_2/(u_{\mathrm{rms}}/\eta)^2 = -0.02$; cyan: $\omega_1 > 0$; yellow: $\omega_1 < 0$, rigid bubble)

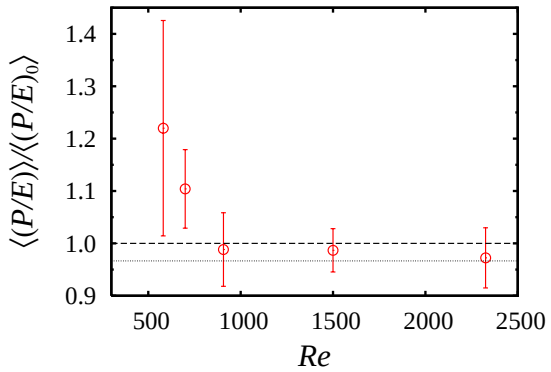

(a) On shear Reynolds number Re (rigid bubble)

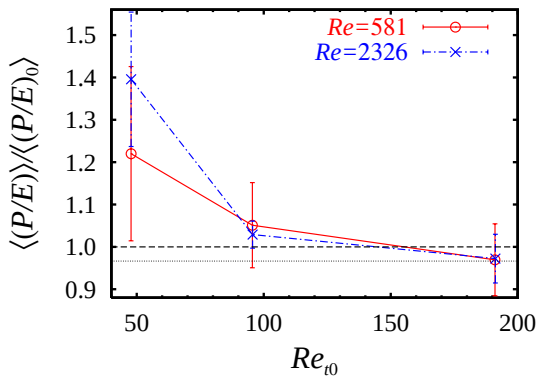

(b) On initial turbulent Reynolds number Re_{t0} (rigid bubble)

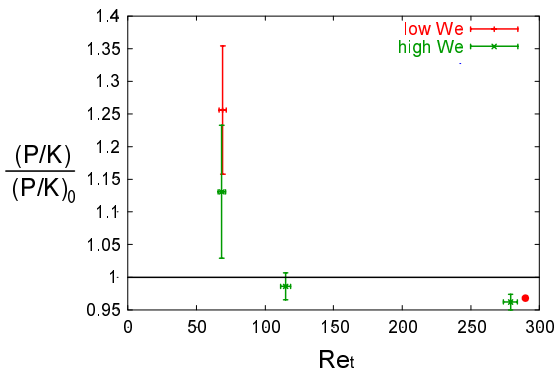

(c) Influence of bubble deformation ($We = 5.0$, 11.5)

Figure 14: Scaled production $\mathcal{P}/E$ ratio